

Super-Resolution Imaging of Self-Assembled Nanocarriers Using Quantitative Spectroscopic Analysis for Cluster Extraction

Janel L. Davis, Yang Zhang, Sijia Yi, Fanfan Du, Ki-Hee Song, Evan A. Scott, Cheng Sun, and Hao F. Zhang*



Cite This: *Langmuir* 2020, 36, 2291–2299



Read Online

ACCESS |



Metrics & More

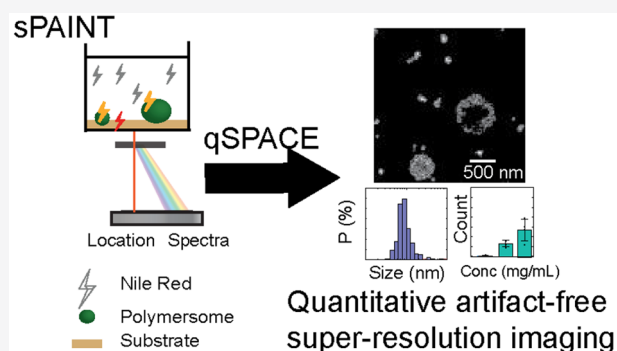


Article Recommendations



Supporting Information

ABSTRACT: Self-assembled nanocarriers have inspired a range of applications for bioimaging, diagnostics, and drug delivery. The noninvasive visualization and characterization of these nanocarriers are important to understand their structure to function relationship. However, the quantitative visualization of nanocarriers in the sample's native environment remains challenging with the use of existing technologies. Single-molecule localization microscopy (SMLM) has the potential to provide both high-resolution visualization and quantitative analysis of nanocarriers in their native environment. However, nonspecific binding of fluorescent probes used in SMLM can introduce artifacts, which imposes challenges in the quantitative analysis of SMLM images. We showed the feasibility of using spectroscopic point accumulation for imaging in nanoscale topography (sPAINT) to visualize self-assembled polymersomes (PS) with molecular specificity. Furthermore, we analyzed the unique spectral signatures of Nile Red (NR) molecules bound to the PS to reject artifacts from nonspecific NR bindings. We further developed quantitative spectroscopic analysis for cluster extraction (qSPACE) to increase the localization density by 4-fold compared to sPAINT; thus, reducing variations in PS size measurements to less than 5%. Finally, using qSPACE, we quantitatively imaged PS at various concentrations in aqueous solutions with ~ 20 nm localization precision and 97% reduction in sample misidentification relative to conventional SMLM.



INTRODUCTION

Nanocarriers are soft nanomaterials with particle sizes typically less than 500 nm in diameter and are frequently used as transport vehicles for other substances.¹ The composition, size, morphology, and functionality of nanocarriers have been extensively investigated for a wide range of biomedical applications, including drug delivery, diagnostics, and therapeutics.¹ The visualization of nanocarriers with minimal perturbation of the nanomaterials and their surrounding environments is a crucial step to understand the relationship between their structure, spatial distribution, and function;^{2,3} however, this remains a challenge with the use of existing imaging techniques. Conventional fluorescence microscopy is unable to fully resolve the nanocarriers because of the optical diffraction limit. Other nonoptical techniques^{4,5} offer higher resolution (e.g., electron microscopy and atomic force microscopy); however, they often require restrictive sample preparations, which alter the sample's native environment. The limitations of the available technologies created the need for a better solution, which can provide high resolution images of nanomaterials in their native environment while simultaneously quantifying their structural and spatial distributions.

Super-resolution optical microscopy allows the visualization of nanomaterials with subdiffraction resolution and molecular specificity.^{2,6–10} In particular, single-molecule localization microscopy (SMLM)^{11–14} techniques detect the stochastic emissions from individual fluorescent molecules, approximate their spatial coordinates with nanometer precision, and reconstruct the image after compiling all the molecular coordinates. For quantitative characterization, sophisticated image processing is required to identify individual nanocarriers and reject background signals coming from, for example, fluorescent impurities or nonspecific labeling. Spatial clustering techniques such as Ripley's K-function,^{15,16} pair correlation,¹⁷ and density-based clustering algorithms^{18–20} have been routinely applied to identify the boundaries of the samples in SMLM.^{21,22} However, Ripley's K-function and pair correlation restrict sample identification to nanocarriers exhibiting homogeneous size distributions. Meanwhile, density-based

Received: October 10, 2019

Revised: February 17, 2020

Published: February 18, 2020

clustering algorithms allow for the identification of a range of samples with inhomogeneous size and shape; however, they are sensitive to background noise and variations in localization density.^{21–23}

Recently developed spectroscopic SMLM or sSMLM^{24–34} techniques distinguish fluorescent signals from individual molecules according to their emission spectra. They provide new strategies for multicolor^{24,25,27–29} and functional super-resolution imaging.^{26,31,35–39} Furthermore, spectral signatures have been used to identify and remove the influence from fluorescent impurities.³⁵ The removal of nonspecific fluorescent signals, however, remains challenging since their spectral signatures are identical to spectral signatures from probes that are bound to the sample. In contrast, a variant of sSMLM referred to as spectroscopic point accumulation for imaging in nanoscale topography (sPAINT)^{26,36,37,39} has been developed to detect specific transient binding of probes, whose fluorescence emission spectra depend on their binding environment. For instance, sPAINT has been employed to image membrane hydrophobicity in liposomes and cells^{26,36} to observe heterogeneity of protein oligomers³⁹ and to characterize the formation of surface adlayers.³⁷

In this work, we demonstrate that sPAINT can be used to quantitatively image and characterize nanocarriers after rejecting nonspecific bindings. We use sPAINT and Nile Red (NR) dye (Figure 1a) to image, count, and measure the size

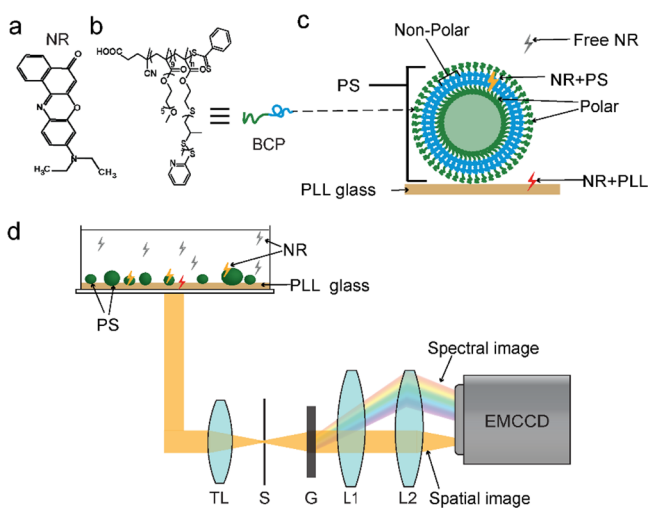


Figure 1. (a) Chemical structure of NR. (b) Chemical structure and illustration of the BCP for PS assembly. (c) Illustration of the assembled PS (the green color represents the polar end of the BCP and the blue color represents the nonpolar end) and the difference in the emission spectra of NR when transiently bound to the PS (yellow) and the PLL-coated glass substrate (red). Free non-fluorescent NR is shown in gray. (d) Schematic of our sPAINT experimental setup. TL: tube lens; S: slit; G: transmission grating; L: lens; EMCCD: electron multiplying charge-coupled device.

distribution of nanocarriers in an aqueous environment, using polymersomes (PS) as a model material. We also report a quantitative Spectroscopic Analysis for Cluster Extraction (qSPACE) postprocessing method to increase the sizing accuracy by optimizing the utilization of the spatial and spectral information obtained from sPAINT. Finally, we validate the accuracy of qSPACE in quantifying the size distribution of PS using nanoparticle tracking analysis (NTA). We also used cryogenic transmission electron microscopy

(cryoTEM) to validate the size range and morphology of the PS in the qSPACE super-resolution image reconstructions.

RESULTS AND DISCUSSION

PS Imaging Using sPAINT. The PS is assembled from block copolymers (BCP) with the nonpolar end facing inward and the polar tails exposed to the aqueous interface (Figure 1b,c).⁴⁰ NR is well-known for its polarity-dependent emission spectrum^{41,42} with unique spectral variations upon binding to PS. Particularly, the bulk emission measurement of NR in aqueous solutions with the presence of PS shows a 55 nm hypsochromic shift in the emission maximum (λ_{\max}) in comparison to those of solutions without PS (Figure S1a).

Figure 1c illustrates the sPAINT imaging principle of PS with NR. The PS sample was immobilized on a poly-L-lysine (PLL) coated glass substrate and imaged in phosphate buffer saline (PBS) solution containing 5 nM NR. The single-molecule blinking signals of free-diffusing NR molecules can only be detected upon transient binding to the PS or PLL substrate. The distinct spectral shifts of the two types of binding events are further distinguished by analyzing the single-molecule spectra using sPAINT. As shown in Figure 1d, the locations and emission spectra of single-molecule signals are concurrently collected after passing through a transmission diffraction grating (see details in the Experimental Section).

A representative sPAINT reconstruction of PS immobilized on the PLL substrate (Figure 2a) shows distinct clustered features (highlighted by 1, 2, and 3), ranging from tens to hundreds of nanometers, and a relatively uniform background with hollow patterns. Using the same concentration of NR, we imaged a control sample (CTRL, PLL substrate without PS). A representative sPAINT reconstruction of the control sample (Figure S1b) shows consistent background patterns without the clustered features, suggesting a large amount of nonspecific bindings of NR to the PLL substrate.

Statistical analysis of 1131 single-molecule spectra collected from 18 clustered features in three different images of the PS sample (Figure S1c–e) showed that the peak of the histograms from the images had a mean λ_{\max} of 610 with a standard deviation of 3 nm (610 ± 3 nm). Three examples of the clustered features are highlighted in Figure 2a, and their corresponding histograms of the λ_{\max} distribution are shown in Figure 2b. To identify nonspecific binding events, we relied on the λ_{\max} values of individual single-molecule emissions from three representative images on the control sample each with $\sim 10^5$ localizations. Figure 2c shows a representative histogram of the λ_{\max} distributions from nonspecific binding events. From the histograms of the three control images, we found that the control sample has two main populations with λ_{\max} of 585 nm ($26 \pm 2\%$) and 645 nm ($57 \pm 2\%$). Using the histograms of λ_{\max} from the PS, we set the peak wavelength for specifically identifying NR interactions with PS as 610 nm. Next, we tested various spectral window (SW) sizes and found that the most efficient SW for rejecting nonspecific binding while specifically identifying NR interactions with PS was from 595–625 nm (see Figure S1g), as highlighted by the red color in Figure 2b,c.

We show three typical single-molecule spectra of NR in Figure 2d. They represent NR specific binding to PS (black curve with λ_{\max} value around 607 nm) and nonspecific binding to PLL substrate (blue and red curves with λ_{\max} values around 571 and 651 nm, respectively). We found that the average single-molecule spectra from the localizations associated with PS matched the bulk measurements of NR in a PBS solution

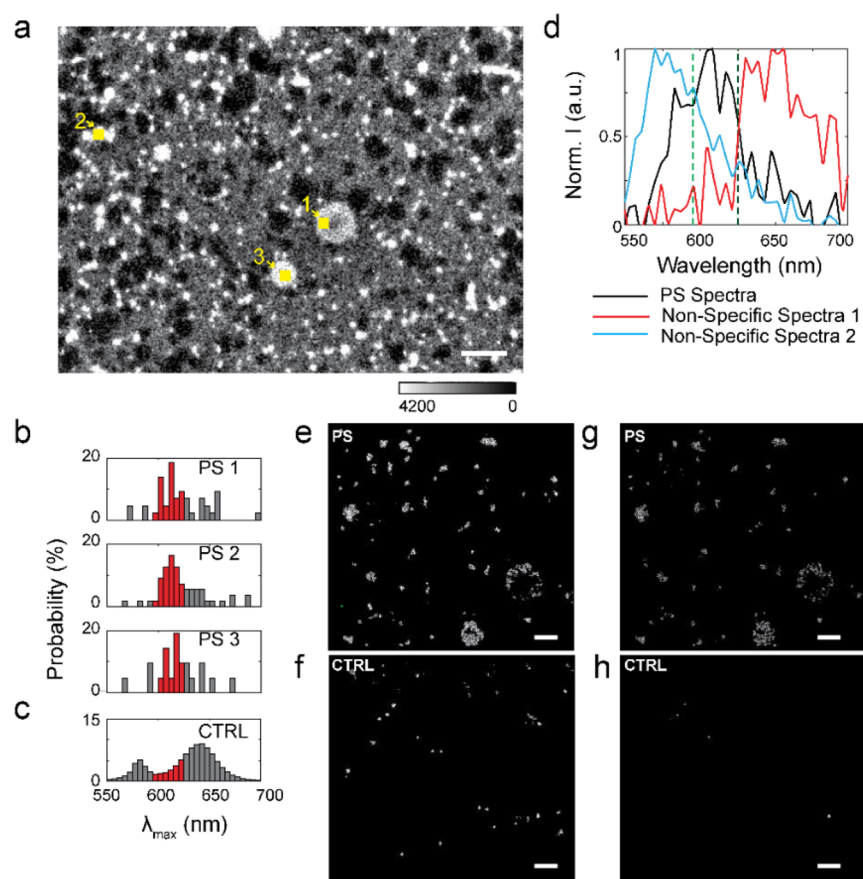


Figure 2. (a) Representative reconstructed super-resolution image of the immobilized the PS sample and NR interactions (scale bar: 1 μm). (b) Histogram of the λ_{max} of NR interactions in three ROIs containing PS as highlighted by the yellow squares numbered 1–3. (c) Histogram of the λ_{max} of nonspecific NR interactions in the control sample. The SW used for detecting NR interactions with PS is highlighted in red. (d) Representative single-molecule spectra from NR+PS binding and nonspecific NR binding (dashed lines indicate the SW). Clusters extracted from (e) the PS sample and (f) control based on DBSCAN alone; clusters extracted from (g) the PS sample and (h) control using sPAINT (scale bar: 500 nm).

containing PS (Figure S1a). Additionally, the average spectra from localizations with $\lambda_{\text{max}} > 645$ nm in the control sample resembled the bulk measurements of NR in solutions without PS (Figure S1a). For sPAINT measurements of the average spectra, 300 localizations from a representative image were used (see the Experimental Section for details). The binding events with $\lambda_{\text{max}} < 595$ nm in the control sample are likely from aggregates of NR in aqueous solutions that are not resolved in the fluorimeter measurements.⁴³

Quantitative analysis of sPAINT images involves two steps. First, we selected localizations within SW (595–625 nm) for PS identification. We confirmed that the NR specific binding to PS can be separated from all other nonspecific binding events using the selected SW (Figure S2). In the control samples, $17 \pm 1\%$ of the localizations had λ_{max} values within the SW. Meanwhile, we found that $58 \pm 5\%$ of the localizations from the clusters in the PS sample were within this SW (Figure S1c). Figure 2b shows examples of the histograms from three regions of interest (ROIs) highlighted in Figure 2a with SW highlighted in red. Histograms of the λ_{max} from ROIs in similar images (Figures S1d,e) show a similar distribution of localizations within SW.

Second, we applied density-based spatial clustering of applications with noise (DBSCAN) optimized for clusters with heterogeneous cluster densities²⁰ to count and size PS. DBSCAN¹⁸ and its variants^{19,20,23} are supervised learning

algorithms which are routinely used for SMLM postprocessing. A cluster radius (CR) and a minimum number of localizations in the CR are user-defined to identify localizations belonging to particular clusters. We defined CR as twice the average localization precision (40 nm).^{23,44} Next, we identified the minimum number of nearest neighbors (min-NN) within the CR of each localization. The localizations were then ordered based on their spatial distribution and grouped into individual clusters.²⁰ Finally, the number of clusters and the size of each cluster was estimated (see details of cluster analysis in the Experimental Section and Figure S3).

We investigated the influence of nonspecific binding on DBSCAN by comparing the number of clusters found by DBSCAN using localizations within SW (sPAINT) and DBSCAN without considering SW. For both cases, only bright localizations that contained high-precision spectral information (localizations at least 450 photons in the spatial domain and average spectral precision ~ 9.2 nm³³) were used. The photon distribution and related spectral precision information for the localizations used in the analysis are shown in Figure S4. We plotted the histograms of the number of nearest neighbors (NN) with and without the SW filter for three different controls and three different PS images (Figure S5). We found that they followed similar distributions. We selected one representative control image and one representative PS image for setting clustering thresholds. For sPAINT and DBSCAN,

we selected min-NN thresholds by achieving the minimal number of clusters from the control sample (see the detailed threshold selection in SI Note 1 and Figures S5g and S6a). Without using SW, we found that DBSCAN was sensitive to nonspecific binding events. We found 55 and 28 clusters with average sizes of 126 and 90 nm in the PS and the control samples, respectively, when performing DBSCAN alone using a min-NN threshold of 20 (Figure 2e,f). In comparison, by first selecting signals within the SW, we found 39 and 3 clusters in the PS and the control samples, respectively, after DBSCAN using a min-NN threshold of 10 (Figure 2g,h). This shows an 89% reduction in the artifacts from nonspecific binding in the control image. While stricter min-NN thresholds can be used to reduce the influence of nonspecific binding using DBSCAN alone, we found that this often causes overfiltering^{16,21,22} which presents an additional challenge since it can erroneously misrepresent the morphology of the sample (Figure S6b).

sPAINT allowed us to image and quantify PS in aqueous environments. Particularly, it enabled the specific detection of NR to PS binding by analyzing the single-molecule emission spectra of each localization event. Meanwhile, sPAINT only used bright localization events (>450 photons in the spatial domain). As a result, clusters identified by sPAINT can have low localization densities (LD, number of localizations in a cluster within the cluster area), which might affect the visualization and size measurement for PS. Therefore, we further investigated the effect of LD on the size measurements and visualization of the PS in sPAINT imaging and further developed a quantitative spectroscopic analysis for cluster extraction (qSPACE) postimaging processing method to increase LD without compromising the specificity achieved by sPAINT in the next section.

Improving Localization Density Using qSPACE. While sPAINT can readily image PS, we recognized that it rejected a large portion of the localization events (Figure S8). In fact, this is a common issue in all sSMLM because the limited photon budget from single-molecule emission events is further split into the spatial and spectral channels.^{24,25,29} Although dim molecules (300–450 photons in the spatial domain) can still be localized at ~25 nm precision (Figure S8), they are discarded since λ_{max} cannot be estimated precisely (estimated spectral precision worse than 15 nm;³³ see SI Note 1 for details) due to their low photon budget.

The limited number of localizations retained by sPAINT could result in clusters with low LD, thus leading to inaccurate measurements of the size and morphology of the PS. Although sPAINT is immune to photobleaching, prolonging the acquisition time to increase the LD has the risk of altering the shape of nanocarriers.^{12,45,46} To address this issue, we developed qSPACE which improved the LD by using the spectroscopic signatures from the PS to guide the recovery of localizations without spectra.

The workflow of qSPACE is shown in Figure 3 (a detailed workflow is shown in Figure S9). First, (i), all the blinking events from the spatial channel are localized after sPAINT imaging. Second, (ii), localizations in SW with bright blinking events (>450 photons in the spatial domain) are selected and DBSCAN is used to generate a high-fidelity validation map of the spatial locations of the true PS sample. Third, (iii), we perform DBSCAN to extract clusters using the localized events from the spatial channel. Then, (iv), we compare the localizations identified by DBSCAN alone, step (iii), to localizations in the validation map, step (ii), to recover

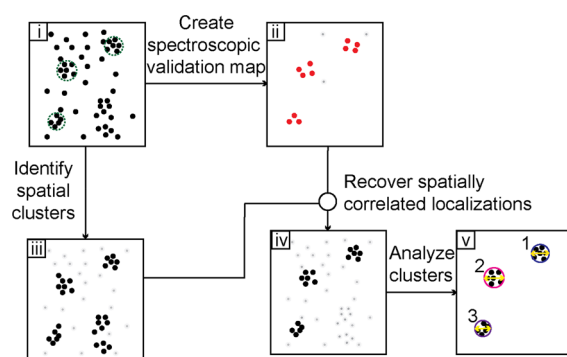


Figure 3. The qSPACE workflow shows the (i) detected spatial localizations with the location of the sample highlighted by the green circles. A subset of localizations containing spectroscopic information is used to create a (ii) validation map that shows clusters with the selected spectra. All detected localizations are used for (iii) spatial clustering without considering spectroscopic information. (iv) Localizations from spatial clusters, which are spatially correlated with the validation map, are recovered for further analysis while artifacts are rejected. (v) The number, size, and morphology of the extracted sample can be further analyzed.

spatially correlated localizations. Localizations identified by DBSCAN alone, which have neighbors in the validation map, are retained and used for qSPACE image reconstruction, while localizations without neighbors are rejected. Finally, step (v), the new clusters with higher localization density can be counted, sized, and visualized.

We quantitatively compared the sizes of PS from a representative image using sPAINT and qSPACE. We first selected 71 identified PS clusters with at least 40 localizations in each cluster to set a criterion for accurate sizing. Using each cluster, we determined the number of localizations which were required for the percent variance in the estimated PS size to drop below 5% (for details, see the Experimental Section, SI Note 2, and Figure S10). We found that, on average, 35 localizations are required to reach a stable PS size. Since the PS varied in size, we used the corresponding LD of $3.5 \times 10^{-3} \text{ nm}^{-2}$ as a threshold to quantify the number of PS with size variations exceeding 5%. In qSPACE, we used a min-NN of 35 to select potential clusters (PC) (Figure S11) and a validation map using sPAINT (SW = [595–625 nm] and min-NN of 10; see additional details for qSPACE parameter selection in SI Note 3 and Figures S11 and S12). Due to the improved LD, all 199 PS identified by qSPACE achieved the LD threshold (Figure 4a). In contrast, 23% of the 187 PS identified by sPAINT alone failed to meet the LD threshold for accurate sizing (Figure 4b).

Additionally, we used the Fourier ring correlation (FRC) to compare the image qualities of the super-resolution reconstructions of PS that were identified using sPAINT alone with further qSPACE processing in a representative image. Although the localization precisions for both methods are comparable (sPAINT: ~20 nm; qSPACE: ~23 nm), the differences in LD affect image resolution.⁴⁷ We calculated the global FRC resolution that takes LD into consideration as previously reported.^{47,48} The FRC resolution is calculated as the inverse of the spatial frequency at a 1/7 of FRC.⁴⁷ We found that qSPACE had a relatively higher FRC resolution of 69 nm while sPAINT had an FRC resolution of 96 nm, as shown in Figure 4c.

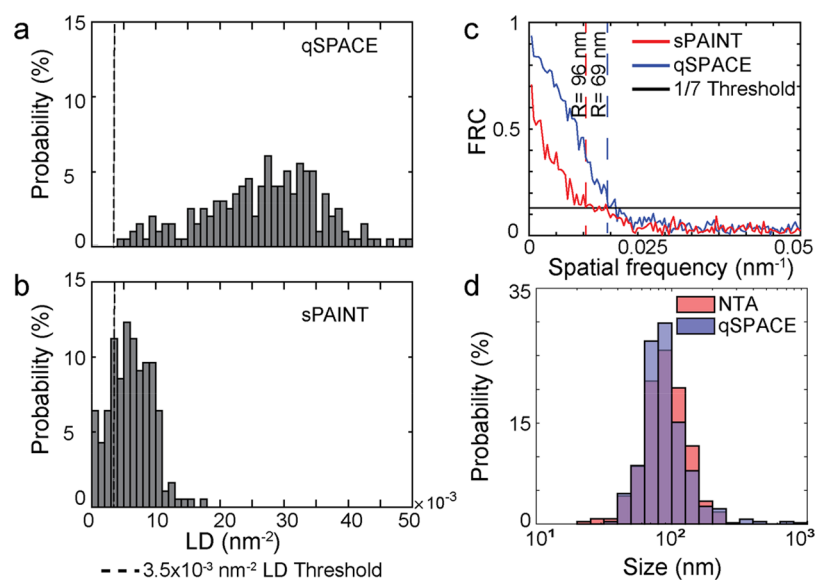


Figure 4. Histograms of the localization densities (black dashed lines indicate the $3.5 \times 10^{-3} \text{ nm}^{-2}$ LD threshold) for (a) qSPACE and (b) sPAINT. (c) Comparison of the global FRC curves for sPAINT (red) and qSPACE (blue). The dashed lines are the corresponding FRC resolution for each method at the 1/7 FRC threshold. (d) Size distribution of PS (0.02 mg/mL) measured by NTA (red) and qSPACE (blue).

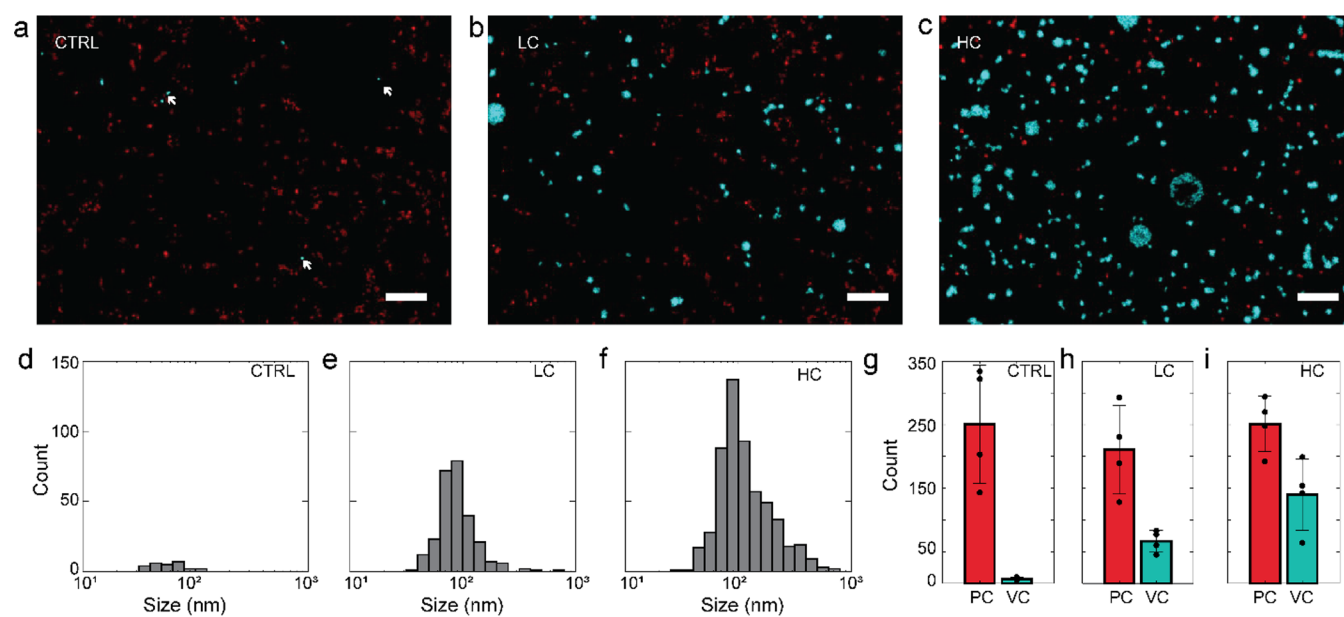


Figure 5. Representative super-resolution reconstructions of the (a) CTRL sample with artifacts pseudocolored in red and misidentified PS pseudocolored in cyan. The three white arrows highlight three examples of sample misidentification. (b) LC sample (0.02 mg/mL) with artifacts pseudocolored in red and validated PS pseudocolored in cyan (scale bar: $1 \mu\text{m}$). The size distributions for the (d) misidentified PS in the CTRL samples, (e) validated PS in the LC samples, and (f) validated PS in the HC samples. Comparison between the total of number of PC found and the qSPACE VC in the (g) CTRL samples, (h) LC samples, and (i) HC samples.

Figure 4d compares the size distributions of 265 PS clusters (0.02 mg/mL) in 4 different images measured by qSPACE and ~ 5000 PS measured by NTA using 5 measurements. The average size of PS measured by qSPACE are $96.6 \pm 2.1 \text{ nm}$. These results agreed well with the average size measured by NTA ($97.6 \pm 1.4 \text{ nm}$). In addition, the cryoTEM image of PS (Figure S13) confirmed that the size of PS ranged from 40 to 200 nm. X-ray scattering analysis also showed consistent results with a core radius of $\sim 106 \text{ nm}$ and shell thickness of $\sim 14.3 \text{ nm}$.⁴⁰ Notably, PS larger than 200 nm, which resulted from the cross-linking process,⁴⁰ were detected by both NTA

(3%) and qSPACE (4%). These validations suggest that qSPACE provides a more accurate size measurement of PS and a higher resolution than sPAINT alone.

Quantitative Characterization of PS at Various Concentrations. Finally, we used qSPACE to visualize, size, and count PS at different concentrations. Figure 5a–c shows representative super-resolution reconstructions of three samples containing 0, 0.02, and 0.2 mg/mL of PS, referred to as control (CTRL), low concentration (LC), and high concentration (HC) samples, respectively. The NR concentration remained constant in these three samples. In the CTRL

image (Figure 5a), the clusters were predominantly identified as artifacts from nonspecific bindings (red color). In the reconstructed LC and HC images (Figure 5b,c), we identified 60 and 199 PS (cyan color), respectively. For statistical analysis, we performed four measurements using different areas of each sample. Figure 5d–f, respectively, shows the size distributions of CTRL, LC, and HC samples. Using qSPACE, we found that the misidentified PS in the control samples have an average size of 63 ± 7.7 nm. The average sizes of identified PS are 137.3 ± 4.8 nm and 96.6 ± 2.1 nm in the HC and LC samples, respectively. Presumably, the aggregation of PS occurs more frequently in the HC samples, thus, resulting in larger PS size.

The counting of PS confirmed the improved performance of qSPACE compared to that of the conventional DBSCAN method. Particularly, 251 ± 93 PC (red bar in Figure 5g) were extracted in the control sample by DBSCAN without spectral analysis while only 7 ± 3 clusters or 3% of these clusters were misidentified as PS by qSPACE (validated clusters or VC, cyan bar in Figure 5g). The average size of the clusters identified as artifacts (clusters correctly rejected by qSPACE) from the control sample was 120.1 ± 4.1 nm. Clusters identified as artifacts in the LC and HC samples had similar distributions (see Figure S14 for the size distribution of artifacts identified by qSPACE and sPAINT). Additionally, 66 ± 18 of 210 ± 70 and 138 ± 56 of 251 ± 44 PC were validated as PS in the LC and HC samples, respectively, using qSPACE (Figure 5h,i).

We compared the relative number of PS in LC to that in HC using qSPACE and NTA. NTA analysis of the two samples indicates a 5-fold higher concentration in HC than in the LC sample. Using qSPACE, we determined the concentration ratio between HC and LC to be ~ 2.1 . The difference in concentration measurements using qSPACE and NTA may come from differences in the sample preparation steps. While NTA measured the entire solution, the samples measured by qSPACE relied on the adhesion of the PS to the PLL substrate. Rinsing steps could also change the relative concentrations of the sample. In short, these results suggest that qSPACE can be used to accurately size and detect the relative trend in the concentration variations of nanocarrier samples.

CONCLUSIONS

We outlined a strategy to quantitatively image and characterize nanocarriers with high specificity, molecular sampling, and ~ 20 nm localization precision. Using sPAINT with NR dye, we successfully imaged PS nanocarriers immobilized on PLL substrates and rejected 83% of nonspecific binding events by identifying the unique spectral signature of NR upon specific binding to PS. We further developed qSPACE to recover the discarded dim localizations in sPAINT to improve LD by 4-fold, reduce variations in size measurements to 5%, and improve the FRC resolution by 30%. By using qSPACE to count and size PS at various concentrations we reduced misidentification of the PS by 97% and validated our results with standard size measurements. qSPACE is not limited to spherical shape clusters and can be used to process distinct morphology. The continued development of fluorescent probes, optical systems, and imaging processing methods for sPAINT would enable the quantitative visualization of polymer assemblies and dynamics in vitro.

EXPERIMENTAL SECTION

Polymersome Preparation. Polymersomes were fabricated based on the self-assembly of amphiphilic brush block copolymers poly(oligo (ethylene glycol) methyl ether methacrylate)-*b*-poly(oligo (propylene sulfide) methacrylate) (POEGMA-POPSMA), which were synthesized based on reversible addition–fragmentation chain transfer (RAFT).⁴⁰ POEGMA-POPS₇MA₈ PS were assembled using the thin-film hydration method as previously described.⁴⁰ Briefly, 20 mg of POEGMA-POPS₇MA₈ copolymer was dissolved in 150 μ L dichloromethane within 1.8 mL clear glass vials (ThermoFisher). After desiccation, to remove the solvent, the resulting thin films were hydrated in 1 mL of phosphate-buffered saline (PBS) under shaking at 1500 rpm overnight. The suspension was then extruded through a 0.2 μ m membrane filter. The cross-linked PS were prepared by the reaction of uncross-linked PS suspension (20 mg/mL) with 1,2-ethanedithiol (36 μ L, 0.15 M in ethanol) through thiol–disulfide exchange reactions under shaking (1500 rpm) at room temperature. The obtained PS were then purified by Zeba Spin Desalting Columns (7K MWCO, ThermoFisher) equilibrated with PBS solution.

Nile Red Preparation. A 3 mM NR (ThermoFisher) stock solution was prepared in dimethylsulfoxide (DMSO) (Sigma-Aldrich). For sPAINT imaging, the solution was further diluted to 5 nM in PBS and used when fresh.

Bulk Fluorescence Measurements. The bulk fluorescence emission spectra of 1 mL solutions containing 1 μ M of NR mixed with 100 μ L of PS (20 mg/mL in PBS), PLL solution (0.01% w/v, Sigma-Aldrich), and PBS, respectively, were measured using a fluorimeter (SpectraMax M3, Molecular Devices). Measurements were recorded using 532 nm excitation.

Sample Immobilization. No. 1 borosilicate four-well Lab-Tek Chambered coverglasses were rinsed three times using PBS, filled with 500 μ L of PLL solution (0.01% w/v, Sigma-Aldrich P4707), and incubated for 30 min to coat the glass surface. The wells were then rinsed three times with PBS. PS was diluted to 0.2 mg/mL (HC sample) and 0.02 mg/mL (LC sample) using PBS. Mixtures of 500 μ L of the HC sample, LC sample, and 500 μ L of PBS (CTRL sample) were transferred to separate 1 mL conical tubes. The three samples were each sonicated for 5 min. The samples were then added to separate wells and incubated for 5 min. The samples were rinsed using PBS. Finally, 500 μ L of freshly prepared 5 nM NR in PBS was sonicated for 5 min and then added to each well for imaging. We also tested bovine albumin serum and neutravidin for sample immobilization chemicals used for the immobilization of biotinylated molecules. However, bulk measurements showed that this immobilization method could provide a larger number of sources for sample misidentification (see Figure S15).

sSMLM Optical Setup. The optical setup contains an inverted optical microscope (Eclipse Ti–U with perfect-focus system, Nikon) equipped with a 532 nm Spectra Physics laser with 200 mW maximum output, a high numerical aperture total internal reflection (TIRF) objective lens (100 \times , NA 1.49, Nikon CFI TIRF apochromat), and a homemade transmission spectrometer. The fluorescence was collected through the objective lens and then directed into a spectrometer consisting of a blazed transmission diffraction grating (300 grooves/mm, Edmund Optics) and two imaging lenses with focal lengths of 100 and 80 mm, respectively. Of the emitted photons, 60% and 40% were, respectively, allocated for the nondispersed zeroth order channel and for the spectrally dispersed first order channel and recorded simultaneously on different regions of an electron multiplying charge-coupled device (EMCCD, ProEm HS 512 \times 3, Princeton Instruments).

Imaging Procedure and Data Analysis. The optical system was calibrated using a fluorescent lamp with the entrance slit adjusted to 10 μ m. The emission peaks at 436.5, 487.7, 546.5, and 611.6 nm were fit with a first order polynomial to calculate the system's spectral dispersion (4.3 nm/pixel). Samples were placed on the microscope stage and imaged using an angle slightly smaller than the TIRF mode. We used a 532 nm laser with a power density of 1 kW/cm² to initiate transient NR binding to PS. An EMCCD camera acquired images

with an integration time of 30 ms. Four areas of the sample were randomly selected and imaged for each sample. For each FOV, 50000 frames were recorded and the spatial image was reconstructed using ThunderSTORM.⁴⁹ ThunderSTORM was used to perform drift correction for each sample prior to spectral analysis. The drift correction file was saved and used to correct all data prior to cluster analysis.^{29,49} Events from overlapping binding events were removed. Additionally, localizations below the average photon count (300) in the spatial image were excluded.

sPAINT Window Selection. Spectroscopic analysis was performed using localizations with a minimum of 450 photons in the spatial domain using an $8 \mu\text{m} \times 7 \mu\text{m}$ section of three different control and three different PS super-resolution reconstructions. The corresponding spectroscopic signature for each localization in the spatial channel was extracted from the first-order images. The emission maximum of each spectroscopic signal was identified by fitting the normalized spectra to a Gaussian.²⁶ Localizations with emission maximums outside the calibration window (550–700 nm) were excluded. The histograms from 18 different PS from three different images (six PS per image) are shown in Figure S1c–e. Examples of emission maximum from three ROIs are shown in Figure 2b. Additionally, the histogram of the emission maximum from the control sample was compared to the PS histograms and a SW (595–625 nm) for recognizing NR interactions with PS and nonspecific binding events was selected. A total of 300 localizations with more than 500 photons in the spectral domain from the isolated PS were used to plot the average spectra in Figure S1a. Similarly, 300 localizations with at least 500 photons in the spectral domain and $\lambda_{\text{max}} > 645 \text{ nm}$ were used to plot the average spectra for NR interactions with PLL.

Cluster Analysis. We adopted a DBSCAN algorithm optimized for clusters with heterogeneous cluster densities.²⁰ Individual PS were identified using a density-based algorithm with a cluster radius of twice the average localization uncertainty (40 nm). NN analysis was performed to determine the minimum number of acceptable localizations within the cluster radius. Localizations that did not meet the minimum criteria were removed. The remaining localizations were sorted based on their NN, Euclidean distance between neighboring points, and spatial coordinates. To consider the influence of the cluster density on the analysis, we used a reachability criterion. If localizations are members of the same cluster, then the variation in the distance between those points will be less than the variation in the distance between points which are members of a different cluster. Using this sorted list, the distance to the next localization in the list is used to identify core and boundary²⁰ localizations of each cluster within a maximum reachable distance of $1 \mu\text{m}$ (based on the maximum PS size⁴⁰). Localizations which were members of a separate cluster were identified when the variation in the distance to the next localization in the sorted list exceeded twice the standard deviation of reachable localizations. The diameter of each cluster was estimated as twice the average distance between the core location and all other localizations in the cluster. To select the min-NN threshold, a range of potential thresholds were tested using both the PS and control samples. The number of clusters resulting from the control relative to the PS sample was used to select the min-NN threshold. Counting accuracy for the algorithm using clusters with varying densities was estimated by a comparison of the reported clusters by algorithm to clusters by manual counting in 10 different $2 \mu\text{m} \times 2 \mu\text{m}$ regions of interest in a representative super-resolution reconstruction.

Quantitative sPAINT Analysis. Cluster analysis using sPAINT relied both on the spectral and spatial information for localizations with at least 450 photons in the spatial domain. The localizations were then further filtered using a min-NN threshold. The performance of spectral analysis paired with spatial clustering was tested by counting the number of clusters in $5 \mu\text{m} \times 5 \mu\text{m}$ sections of representative PS and control super-resolution reconstructions with and without applying the SW (595–625 nm). A min-NN of 10 was selected for cluster analysis after application of the SW, and a min-NN of 20 was selected for cluster analysis without applying the SW. The numbers and sizes of artifacts found by sPAINT (Figure S14b) were identified

using localizations which were not in SW and not spatially correlated with any of the clusters using the SW filter.

Size Variation Analysis. We measured the effect of the reduced number of localizations per cluster on size measurements by selecting 71 sPAINT clusters with at least 40 localizations. We calculated the difference between the final size of the cluster and the size of the cluster as the number of localizations sequentially increased. The percent variance in the size was calculated as the ratio of the difference in size measurements as the number of localizations increased and the final size of the cluster. This trend was further investigated by grouping the analyzed clusters based on their varying sizes. To account for the different sizes of PS, we set a criterion for evaluating size measurements based on the localization density (LD, the number of localizations in a cluster divided by the PS cluster area detected using sPAINT).

qSPACE Validation. The validation map for qSPACE was created using the localizations after applying the SW (595–625 nm) and removing isolated localizations (min-NN of 10). Potential spatial clusters were identified by applying a weak min-NN threshold (35) to all localizations with at least 300 photons in the spatial domain. The spatial coordinates of the localizations, which formed spatial clusters, were compared to those in the validation map. Localizations that did not have any neighbors in the validation map were marked as artifacts. The remaining spatial localizations were used for counting and sizing as described in the Cluster Analysis section. For the qSPACE super-resolution reconstructions in Figure 5, all clusters were pseudocolored based on their classification. The final qSPACE analysis was performed using 12 different $11 \times 8 \mu\text{m}^2$ images acquired from 3 samples. Four measurements were captured from each sample.

Nanosight Measurements. The size distribution of a $1:10^4$ dilution of the stock PS solution was measured using nanoparticle tracking analysis (Nanosight NS300, Malvern). We also tested the relative concentration of the high concentration and low concentration samples by testing $1:10^3$ dilutions of the samples used in the sPAINT experiment. All Nanosight measurements were performed using an unlabeled sample and a 488 nm excitation source, and five trials were performed with statistical analysis using NTA.

CryoTEM Measurements. Cryogenic transmission electron microscopy (cryoTEM) of the PS samples was performed as previously described.⁴⁰ A $4 \mu\text{L}$ portion of a 5 mg/mL sample was applied to a pretreated, lacey carbon 400 mesh TEM copper grid (Electron Microscopy Sciences). The grids were plunge-frozen with a Gatan Cryoplunge freezer at room temperature. Images were collected using a JEOL 3200FSC transmission electron microscope.

■ ASSOCIATED CONTENT

SI Supporting Information

The following file is available free of charge. The Supporting Information is available free of charge at <https://pubs.acs.org/doi/10.1021/acs.langmuir.9b03149>.

Experimental data and details containing the average sSMLM and bulk emission spectra of polymersomes and immobilization chemicals, sSMLM images of the control sample, spectral window selection, density-based clustering algorithm optimization, size measurement analysis, qSPACE workflow and optimization, cryoTEM image of polymersomes, and size distribution of imaging artifacts (PDF)

■ AUTHOR INFORMATION

Corresponding Author

Hao F. Zhang – Department of Biomedical Engineering, Northwestern University, Evanston, Illinois 60208, United States; Email: hfzhang@northwestern.edu

Authors

Janel L. Davis – Department of Biomedical Engineering, Northwestern University, Evanston, Illinois 60208, United States; orcid.org/0000-0001-6645-0758

Yang Zhang – Department of Biomedical Engineering, Northwestern University, Evanston, Illinois 60208, United States; orcid.org/0000-0003-1011-3001

Sijia Yi – Department of Biomedical Engineering, Northwestern University, Evanston, Illinois 60208, United States

Fanfan Du – Department of Biomedical Engineering, Northwestern University, Evanston, Illinois 60208, United States

Ki-Hee Song – Department of Biomedical Engineering, Northwestern University, Evanston, Illinois 60208, United States; orcid.org/0000-0002-1077-2667

Evan A. Scott – Department of Biomedical Engineering, Northwestern University, Evanston, Illinois 60208, United States; orcid.org/0000-0002-8945-2892

Cheng Sun – Department of Mechanical Engineering, Northwestern University, Evanston, Illinois 60208, United States; orcid.org/0000-0002-2744-0896

Complete contact information is available at:

<https://pubs.acs.org/10.1021/acs.langmuir.9b03149>

Notes

The authors declare no competing financial interest.

ACKNOWLEDGMENTS

This work was supported by NSF Grant Nos. CBET-1706642, EFRI-1830969, and EEC-1530734 and by NIH grants R01EY026078, R01EY029121, and DP2HL132390. J.L.D. was supported by the NSF Graduate Research Fellowship DGE-1842165. Nanoparticle tracking analysis was performed in the Analytical bioNanoTechnology Core Facility of the Simpson Querrey Institute at Northwestern University. The U.S. Army Research Office, the U.S. Army Medical Research and Materiel Command, and Northwestern University provided funding to develop this facility, and ongoing support is being received from the Soft and Hybrid Nanotechnology Experimental (SHyNE) Resource (NSF ECCS-1542205).

REFERENCES

- (1) Allen, S. D.; Bobbala, S.; Karabin, N. B.; Scott, E. A. On the advancement of polymeric bicontinuous nanospheres toward biomedical applications. *Nanoscale Horiz.* **2019**, *4* (2), 258–272.
- (2) Pujals, S.; Feiner-Gracia, N.; Delcanale, P.; Voets, I.; Albertazzi, L. Super-resolution microscopy as a powerful tool to study complex synthetic materials. *Nat. Rev. Chem.* **2019**, *3* (2), 68–84.
- (3) Habel, J.; Ogbonna, A.; Larsen, N.; Cherre, S.; Kynde, S.; Midtgaard, S. R.; Kinoshita, K.; Krabbe, S.; Jensen, G. V.; Hansen, J. S.; Almdal, K.; Helix-Nielsen, C. Selecting analytical tools for characterization of polymersomes in aqueous solution. *RSC Adv.* **2015**, *5* (97), 79924–79946.
- (4) Patterson, J. P.; Xu, Y. F.; Moradi, M. A.; Sommerdijk, N. A. J. M.; Friedrich, H. CryoTEM as an Advanced Analytical Tool for Materials Chemists. *Acc. Chem. Res.* **2017**, *50* (7), 1495–1501.
- (5) Binnig, G.; Quate, C. F.; Gerber, C. Atomic Force Microscope. *Phys. Rev. Lett.* **1986**, *56* (9), 930–933.
- (6) Boott, C. E.; Laine, R. F.; Mahou, P.; Finnegan, J. R.; Leitao, E. M.; Webb, S. E. D.; Kaminski, C. F.; Manners, I. In Situ Visualization of Block Copolymer Self-Assembly in Organic Media by Super-Resolution Fluorescence Microscopy. *Chem. - Eur. J.* **2015**, *21* (51), 18539–18542.

(7) Qiu, H. B.; Gao, Y.; Boott, C. E.; Gould, O. E. C.; Harniman, R. L.; Miles, M. J.; Webb, S. E. D.; Winnik, M. A.; Manners, I. Uniform patchy and hollow rectangular platelet micelles from crystallizable polymer blends. *Science* **2016**, *352* (6286), 697–701.

(8) Woll, D.; Flors, C., Super-resolution Fluorescence Imaging for Materials Science. *Small Methods* **2017**, *1* (10), 1700191

(9) Albertazzi, L.; van der Zwaag, D.; Leenders, C. M. A.; Fitzner, R.; van der Hofstad, R. W.; Meijer, E. W. Probing Exchange Pathways in One-Dimensional Aggregates with Super-Resolution Microscopy. *Science* **2014**, *344* (6183), 491–495.

(10) Aloï, A.; Vargas Jentsch, A.; Vilanova, N.; Albertazzi, L.; Meijer, E. W.; Voets, I. K. Imaging Nanostructures by Single-Molecule Localization Microscopy in Organic Solvents. *J. Am. Chem. Soc.* **2016**, *138* (9), 2953–2956.

(11) Betzig, E.; Patterson, G. H.; Sougrat, R.; Lindwasser, O. W.; Olenych, S.; Bonifacino, J. S.; Davidson, M. W.; Lippincott-Schwartz, J.; Hess, H. F. Imaging intracellular fluorescent proteins at nanometer resolution. *Science* **2006**, *313* (5793), 1642–1645.

(12) Sharonov, A.; Hochstrasser, R. M. Wide-field subdiffraction imaging by accumulated binding of diffusing probes. *Proc. Natl. Acad. Sci. U. S. A.* **2006**, *103* (50), 18911–18916.

(13) Rust, M. J.; Bates, M.; Zhuang, X. W. Sub-diffraction-limit imaging by stochastic optical reconstruction microscopy (STORM). *Nat. Methods* **2006**, *3* (10), 793–795.

(14) Zhang, Y.; Song, K. H.; Tang, S. C.; Ravelo, L.; Cusido, J.; Sun, C.; Zhang, H. F.; Raymo, F. M. Far-Red Photoactivatable BODIPYs for the Super-Resolution Imaging of Live Cells. *J. Am. Chem. Soc.* **2018**, *140* (40), 12741–12745.

(15) Ripley, B. D. Modeling Spatial Patterns. *J. R. Stat. Soc. B. Met.* **1977**, *39* (2), 172–212.

(16) Rubin-Delanchy, P.; Burn, G. L.; Griffie, J.; Williamson, D. J.; Heard, N. A.; Cope, A. P.; Owen, D. M. Bayesian cluster identification in single-molecule Localization microscopy data. *Nat. Methods* **2015**, *12* (11), 1072–1076.

(17) Sengupta, P.; Jovanovic-Taliman, T.; Skoko, D.; Renz, M.; Veatch, S. L.; Lippincott-Schwartz, J. Probing protein heterogeneity in the plasma membrane using PALM and pair correlation analysis. *Nat. Methods* **2011**, *8* (11), 969–975.

(18) Ester, M.; Kriegel, H.-P.; Sander, J.; Xu, X. A density-based algorithm for discovering clusters a density-based algorithm for discovering clusters in large spatial databases with noise. *Proceedings of the Second International Conference on Knowledge Discovery and Data Mining*, AAAI Press: Portland, OR, 1996; pp 226–231.

(19) Achtert, E.; Bohm, C.; Kroger, P. DeLiClu: Boosting robustness, completeness, usability, and efficiency of hierarchical clustering by a closest pair ranking. *Lect. Notes Artif. Int.* **2006**, *3918*, 119–128.

(20) Ankerst, M.; Breunig, M. M.; Kriegel, H. P.; Sander, J. OPTICS: Ordering points to identify the clustering structure. *Sigmod Record, Vol 28, No 2 - June 1999* **1999**, *28*, 49–60.

(21) Nicovich, P. R.; Owen, D. M.; Gaus, K. Turning single-molecule localization microscopy into a quantitative bioanalytical tool. *Nat. Protoc.* **2017**, *12* (3), 453–460.

(22) Levet, F.; Hosity, E.; Kechkar, A.; Butler, C.; Beghin, A.; Choquet, D.; Sibarita, J. B. SR-Tesseler: a method to segment and quantify localization-based super-resolution microscopy data. *Nat. Methods* **2015**, *12* (11), 1065–1071.

(23) Mazouchi, A.; Milstein, J. N. Fast Optimized Cluster Algorithm for Localizations (FOCAL): a spatial cluster analysis for super-resolved microscopy. *Bioinformatics* **2016**, *32* (5), 747–54.

(24) Zhang, Z. Y.; Kenny, S. J.; Hauser, M.; Li, W.; Xu, K. Ultrahigh-throughput single-molecule spectroscopy and spectrally resolved super-resolution microscopy. *Nat. Methods* **2015**, *12* (10), 935–938.

(25) Dong, B. Q.; Almassalha, L.; Urban, B. E.; Nguyen, T. Q.; Khuon, S.; Chew, T. L.; Backman, V.; Sun, C.; Zhang, H. F. Super-resolution spectroscopic microscopy via photon localization. *Nat. Commun.* **2016**, *7*, 12290 DOI: [10.1038/ncomms12290](https://doi.org/10.1038/ncomms12290).

(26) Bongiovanni, M. N.; Godet, J.; Horrocks, M. H.; Tosatto, L.; Carr, A. R.; Wirthensohn, D. C.; Ranasinghe, R. T.; Lee, J. E.;

- Ponjavic, A.; Fritz, J. V.; Dobson, C. M.; Klenerman, D.; Lee, S. F. Multi-dimensional super-resolution imaging enables surface hydrophobicity mapping. *Nat. Commun.* **2016**, *7*, 13544 DOI: 10.1038/ncomms13544.
- (27) Mlodzianowski, M. J.; Curthoys, N. M.; Gunewardene, M. S.; Carter, S.; Hess, S. T. Super-Resolution Imaging of Molecular Emission Spectra and Single Molecule Spectral Fluctuations. *PLoS One* **2016**, *11* (3), e0147506.
- (28) Huang, T.; Phelps, C.; Wang, J.; Lin, L. J.; Bittel, A.; Scott, Z.; Jacques, S.; Gibbs, S. L.; Gray, J. W.; Nan, X. L. Simultaneous Multicolor Single-Molecule Tracking with Single-Laser Excitation via Spectral Imaging. *Biophys. J.* **2018**, *114* (2), 301–310.
- (29) Zhang, Y.; Song, K. H.; Dong, B. Q.; Davis, J. L.; Shao, G. B.; Sun, C.; Zhang, H. F. Multicolor super-resolution imaging using spectroscopic single-molecule localization microscopy with optimal spectral dispersion. *Appl. Opt.* **2019**, *58* (9), 2248–2255.
- (30) Dong, B. Q.; Davis, J. L.; Sun, C.; Zhang, H. F. Spectroscopic analysis beyond the diffraction limit. *Int. J. Biochem. Cell Biol.* **2018**, *101*, 113–117.
- (31) Urban, B. E.; Dong, B. Q.; Nguyen, T. Q.; Backman, V.; Sun, C.; Zhang, H. F. Subsurface Super-resolution Imaging of Unstained Polymer Nanostructures. *Sci. Rep.-Uk* **2016**, *6*.
- (32) Yan, R.; Moon, S.; Kenny, S. J.; Xu, K. Spectrally Resolved and Functional Super-resolution Microscopy via Ultrahigh-Throughput Single-Molecule Spectroscopy. *Acc. Chem. Res.* **2018**, *51* (3), 697–705.
- (33) Song, K. H.; Dong, B. Q.; Sun, C.; Zhang, H. F. Theoretical analysis of spectral precision in spectroscopic single-molecule localization microscopy. *Rev. Sci. Instrum.* **2018**, *89* (12), 123703.
- (34) Song, K. H.; Zhang, Y.; Wang, G. X.; Sun, C.; Zhang, H. F. Three-dimensional biplane spectroscopic single-molecule localization microscopy. *Optica* **2019**, *6* (6), 709–715.
- (35) Davis, J. L.; Dong, B. Q.; Sun, C.; Zhang, H. F. Method to identify and minimize artifacts induced by fluorescent impurities in single-molecule localization microscopy. *J. Biomed. Opt.* **2018**, *23* (10), 1.
- (36) Moon, S.; Yan, R.; Kenny, S. J.; Shyu, Y.; Xiang, L. M.; Li, W.; Xu, K. Spectrally Resolved, Functional Super-Resolution Microscopy Reveals Nanoscale Compositional Heterogeneity in Live-Cell Membranes. *J. Am. Chem. Soc.* **2017**, *139* (32), 10944–10947.
- (37) Xiang, L. M.; Wojcik, M.; Kenny, S. J.; Yan, R.; Moon, S.; Li, W.; Xu, K. Optical characterization of surface adlayers and their compositional demixing at the nanoscale. *Nat. Commun.* **2018**, *9*, 3820 DOI: 10.1038/s41467-018-03820-w.
- (38) Kim, D.; Zhang, Z. Y.; Xu, K. Spectrally Resolved Super-Resolution Microscopy Unveils Multipath Reaction Pathways of Single Spiropyran Molecules. *J. Am. Chem. Soc.* **2017**, *139* (28), 9447–9450.
- (39) Lee, J. E.; Sang, J. C.; Rodrigues, M.; Carr, A. R.; Horrocks, M. H.; De, S.; Bongiovanni, M. N.; Flagmeier, P.; Dobson, C. M.; Wales, D. J.; Lee, S. F.; Klenerman, D. Mapping Surface Hydrophobicity of alpha-Synuclein Oligomers at the Nanoscale. *Nano Lett.* **2018**, *18* (12), 7494–7501.
- (40) Du, F. F.; Bobbala, S.; Yi, S. J.; Scott, E. A. Sequential intracellular release of water-soluble cargos from Shell-crosslinked polymersomes. *J. Controlled Release* **2018**, *282*, 90–100.
- (41) Greenspan, P.; Fowler, S. D. Spectrofluorometric Studies of the Lipid Probe, Nile Red. *J. Lipid Res.* **1985**, *26* (7), 781–789.
- (42) Greenspan, P.; Mayer, E. P.; Fowler, S. D. Nile Red - a Selective Fluorescent Stain for Intracellular Lipid Droplets. *J. Cell Biol.* **1985**, *100* (3), 965–973.
- (43) Dutta, A. K.; Kamada, K.; Ohta, K. Spectroscopic studies of Nile red in organic solvents and polymers. *J. Photochem. Photobiol., A* **1996**, *93* (1), 57–64.
- (44) Owen, D. M.; Rentero, C.; Rossy, J.; Magenau, A.; Williamson, D.; Rodriguez, M.; Gaus, K. PALM imaging and cluster analysis of protein heterogeneity at the cell surface. *J. Biophotonics* **2010**, *3* (7), 446–454.
- (45) Salva, R.; Le Meins, J. F.; Sandre, O.; Brulet, A.; Schmutz, M.; Guenoun, P.; Lecommandoux, S. Polymersome Shape Transformation at the Nanoscale. *ACS Nano* **2013**, *7* (10), 9298–9311.
- (46) Rikken, R. S. M.; Engelkamp, H.; Nolte, R. J. M.; Maan, J. C.; van Hest, J. C. M.; Wilson, D. A.; Christianen, P. C. M. Shaping polymersomes into predictable morphologies via out-of-equilibrium self-assembly. *Nat. Commun.* **2016**, *7*, 12606 DOI: 10.1038/ncomms12606.
- (47) Nieuwenhuizen, R. P. J.; Lidke, K. A.; Bates, M.; Puig, D. L.; Grunwald, D.; Stallinga, S.; Rieger, B. Measuring image resolution in optical nanoscopy. *Nat. Methods* **2013**, *10* (6), 557–562.
- (48) Culley, S.; Albrecht, D.; Jacobs, C.; Pereira, P. M.; Leterrier, C.; Mercer, J.; Henriques, R. Quantitative mapping and minimization of super-resolution optical imaging artifacts. *Nat. Methods* **2018**, *15* (4), 263–266.
- (49) Ovesny, M.; Krizek, P.; Borkovec, J.; Svindrych, Z. K.; Hagen, G. M. ThunderSTORM: a comprehensive ImageJ plug-in for PALM and STORM data analysis and super-resolution imaging. *Bioinformatics* **2014**, *30* (16), 2389–2390.